Image Quality Comparison between Synthetic 2D Mammograms Obtained with 15° and 40° X-ray Tube Angular Range: A Quantitative Phantom Study

R. Lamastra[1,2], P. Barca[1,2], M. G. Bisogni[1,2], D. Caramella[3], V. Rosso[1,2], R. M. Tucciariello[1,2], A. C. Traino[4] and M. E. Fantacci[1,2]

[1]*Department of Physics, University of Pisa, Pisa, Italy*
[2]*INFN, Pisa Section, Pisa, Italy*
[3]*Department of Translational Research on New Technologies in Medicine and Surgery, University of Pisa, Pisa, Italy*
[4]*Unit of Medical Physics, Pisa University Hospital "Azienda Ospedaliero-Universitaria Pisana", Pisa, Italy*

Keywords: Synthesized Mammography, Digital Breast Tomosynthesis, Image Quality, Angular Range.

Abstract: In this work we present an image quality comparison between synthesized mammograms (SMs) obtained from Digital Breast Tomosynthesis (DBT) acquisitions with 15° (SM_{15}) and 40° (SM_{40}) X-ray tube angular range. In fact, since wide-angle DBT is characterized by a better spatial resolution in depth but also by worse performance in detecting microcalcifications than narrow-angle DBT, an objective image quality analysis of SM images could be of pratical interest. Four phantoms were employed in this study and their images were acquired using an Amulet Innovality mammographic device. The image quality comparison was conducted by evaluating spatial resolution, contrast and noise properties of the images. Our results show that SM_{40} images are characterized by better spatial resolution performance than SM_{15} in terms of Modulation Transfer Function but also by worse performance in the detection of low-contrast details. In fact, higher contrast-to-noise ratio values were obtained with SM_{15} than with SM_{40}. Noise properties of the images were also investigated through the Noise Power Spectrum (NPS) calculation: no differences in NPS shapes were found in both modalities, while noise magnitude results significantly different. In addition, Signal-to-Noise Ratio (SNR) spatial distribution evaluation was assessed by computing SNR maps, in which different pattern were observed.

1 INTRODUCTION

Digital Breast Tomosynthesis (DBT) is a pseudo-3D X-ray breast imaging method that reduces the tissue superposition problems associated with 2D Digital Mammography (DM), facilitating discrimination between normal tissue and lesions (Sechopoulos et al., 2013; Sechopoulos et al., 2013; Vedantham et al., 2015).

In DBT modality, the X-ray tube rotates along a fixed axis through a limited angular range and a projection of the compressed breast is acquired every few degrees. Starting from these projections data, a set of fixed-thickness image planes is reconstructed applying filter back-projection or iterative algorithm (Vedantham et al., 2015). The resulting reconstructed images are characterized by a poor spatial resolution in depth due to the limited angular range (Marshall et al., 2012; Sechopoulos et al., 2013).

In recent years, a number of DBT systems have been developed with different geometries and technical characteristics. In particular, some systems offer the possibility to adopt different angular range of acquisition. Generally, devices with a wide angular range express a better spatial resolution in depth than those equipped with a narrow angular range (Marshall et al., 2012; Yoshinari et al., 2014). In this regard, Chan et al. have shown that wide-angle DBT allows a better identification of the breast lesions (Chan et al., 2017). On the other hand, other studies concluded that narrow-angle DBT performs better than wide-angle DBT in the identification of microcalcifications (Chan et al., 2014; Hadjipanteli et al., 2016).

However, although DBT allows a tissue separation along the z axis, the in-plane spatial

Lamastra, R., Barca, P., Bisogni, M., Caramella, D., Rosso, V., Tucciariello, R., Traino, A. and Fantacci, M.
Image Quality Comparison between Synthetic 2D Mammograms Obtained with 15° and 40° X-ray Tube Angular Range: A Quantitative Phantom Study.
DOI: 10.5220/0009147601840191
In *Proceedings of the 13th International Joint Conference on Biomedical Engineering Systems and Technologies (BIOSTEC 2020) - Volume 2: BIOIMAGING*, pages 184-191
ISBN: 978-989-758-398-8; ISSN: 2184-4305

resolution of the DBT images is generally worse than the spatial resolution of a DM image (Marshall et al., 2012; Mackenzie et al., 2017); so radiologists could have greater difficulty in detecting microcalcifications, if only DBT images are examinated. Several studies showed that DM modality is the procedure with the best performance in detecting microcalcifications (Rodriguez-Ruiz et al., 2016; Rose et al., 2013; Hadjipanteli et al., 2017). Therefore, DBT has been employed in conjunction to DM acquisition to increase the diagnostic accuracy, i.e. specificity and sensitivity (Houssami, 2018; Shin et al., 2014; Svahn et al., 2010). However, the combined use of DBT with DM procedure leads to a relevant increase in breast absorbed dose and in breast compression time compared to DM or DBT alone (Durand, 2018; Zuckerman et al., 2017; Alshafeiy et al., 2017). To avoid a DM extra acquisition and reduce the total dose to the patient, manufacturers have recently introduced the "synthesized mammograms" (SMs): projection-like images obtained by combining the DBT data (Durand, 2018; Zuckerman et al., 2017; Smith, 2015).

Since wide-angle DBT is characterized by a better spatial resolution in depth but also by worse performance in detecting microcalifications with respect to narrow-angle DBT, SM images could play an important role as a support for DBT examinations.

Therefore, in order to better determine which could be the more appropriate approach to adopt for investigating a given clinical task, a comparison between SMs obtained with wide and narrow angle is essential. In this context, the aim of our study is to compare the image quality between the SMs in wide-DBT and those obtained in narrow-DBT modality.

2 MATERIALS AND METHODS

An Amulet Innovality (Fujifilm Medical System USA Inc., USA) mammographic device was employed in this phantom-study for acquiring SM images in different X-ray tube angular ranges.

The Amulet Innovality model allows the selection of two different DBT acquisition modes: the standard (ST) mode, which uses a narrow angular range of projections (15°), and the high resolution (HR) mode, which uses a wide angular range of projections (40°). SM images obtained in ST and HR mode are characterized by pixel dimensions of 0.15 mm and 0.10 mm respectively.

Four different phantoms were used in this study for quantitatively investigating the image quality of SM images obtained from DBT acquisitions with 15° (SM_{15}) and 40° (SM_{40}) X-ray tube angular range. The phantoms were imaged by using the exposure parameters closest to the automatic exposure (AE) settings related to 4 cm thick PMMA slab phantom (31 kVp and 36 mAs for 15° and 31 kVp and 42 mAs for 40° case).

The image quality comparison between the SM_{15} and SM_{40} was performed by evaluating: the Modulation Transfer Function (MTF), the Contrast-to-Noise Ratio (CNR), the Noise Power Spectrum (NPS) and maps of Signal-to-Noise Ratio (SNR).

For spatial resolution evaluation, a home-made phantom with a tungsten wire of 12.5 µm diameter (Fig. 1) was specifically assembled. The tungsten wire was tilted by about 3 degrees and was placed on 1 mm thick PMMA slab.

Figure 1: Image of the home-made phantom (4 x 2 cm^2) with a tungsten wire tilted by about 3 degrees employed to evaluate the Line Spread Function.

In order to simulate a standard 4.5 cm thick breast, a 4 cm thick PMMA slab was placed above the home made phantom (EUREF, 2006). Spatial resolution was assessed by calculating the MTF through the Line Spread Function (LSF) approach (EUREF 2016). A series of profiles were extracted and combined to obtain the over-sampled LSF. Then, a Gaussian fit was performed and finally the Fourier Transform was applied. The MTF was calculated along the tube-motion direction for both modes, in order to investigate the influence of the angular range on the spatial resolution of the system.

The CNR evaluation was performed examining the four larger masses of the ACR phantom (Fluke Biomedical, Everett, WA, USA, Fig. 2) and the 6 groups of low-contrast inserts of the TORMAM phantom (Leeds Test Objects Ltd, North Yorkshire, UK, Fig. 3).

To reproduce the standard 4.5 cm thick breast, the TORMAM phantom was placed on top of a 2.5 cm thick PMMA plate, while the ACR phantom was positioned directly on the breast support plate

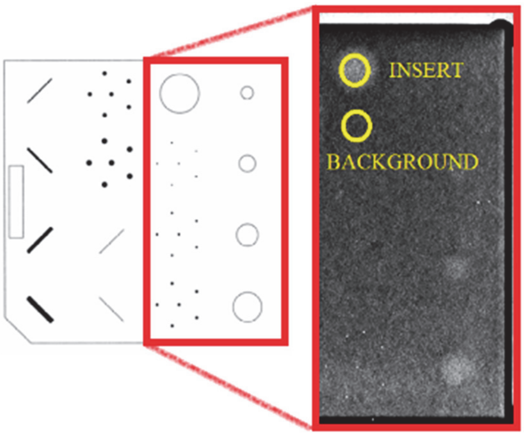

Figure 2: On the left, a detailed picture of the whole ACR mammographic phantom is presented; on the right, an SM image of the ACR phantom is highlighted in red. An example of circular region of interests employed for the CNR calculation is also shown.

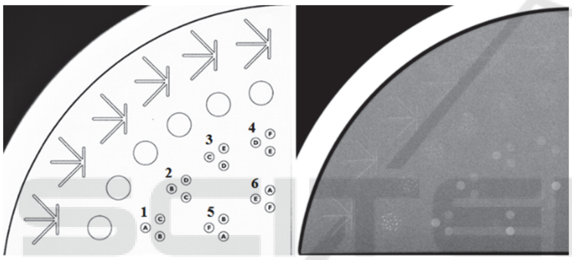

Figure 3: On the left, a detailed picture of the TORMAM phantom is presented; on the right, an SM image of the 6 groups of low-contrast inserts of the TORMAM phantom is shown.

(EUREF 2006; EFOMP 2015; Fluke Biomedical 2005). For the CNR calculation, the following relationship was adopted (Goodsitt MM et al., 2014):

$$CNR = \frac{PV_{insert} - PV_{background}}{\sigma_{background}} \quad (1)$$

where PV_{insert} and $PV_{background}$ are the mean pixel values in a region of interest (ROI) placed within the insert and in the background region respectively; $\sigma_{background}$ is the standard deviation computed in the background ROI. Circular ROIs of 15 and 23 pixels in diameters were used for CNR analysis in the TORMAM phantom for SM_{15} and SM_{40} respectively. These ROI diameters correspond to a spatial dimension of about 2.3 mm. Conversely, since the ACR inserts are of different sizes, the ROI dimensions were adapted to the size of the each detail. For each phantom, three acquisitions were performed adopting the same exposure parameters; the average and the standard deviation were then calculated.

A 4 cm thick PMMA plate (30x24x4 cm^3) was employed to study the noise spectral properties of the system. Specifically, noise properties of SM_{15} and SM_{40} were investigated through the calculation of the NPS. The NPS was computed by applying the Siewerdsen approach (Siewerdsen et al., 2002). A set of radial profiles of the 2D NPS was extracted from a circular ROI centered to the origin of the frequency space. The dimension of the ROI radius was fixed to the Nyquist frequency. The average of the radial profiles was then calculated to better visualize the shape of the spectrum.

Besides, to further investigate the noise properties of SMs, SNR maps were calculated averaging 30 acquisitions of the homogeneous 4 cm thick PMMA phantom. Starting from these 30 acquisitions, the average and the standard deviation (SD) across the image set were computed for each pixel to determine average and SD maps. SNR maps were obtained from the ratio between the average map and the SD map. Finally, the SNR map was normalized to the maximum value. To quantify the differences in SNR maps, the following non-uniformity index (NUI) was adopted:

$$NUI = \frac{\max(PV_{ROI_i}) - \min(PV_{ROI_i})}{\left[\dfrac{\max(PV_{ROI_i}) + \min(PV_{ROI_i})}{2}\right]} \quad (2)$$

where PV_{ROI_i} is the mean pixel value within the i_{th}-ROI. This index was evaluated on a ROI selected from the obtained SNR map and by excluding about 1 cm from the edge to avoid edge effects. The NUI was computed by considering a set of sub-ROIs of 100x100 pixels spanning the whole image. For each sub-ROI, the mean pixel value was calculated and then the minimum and maximum values were employed in Eq. (2).

Image analysis was performed by using ImageJ (Wayne Rasband, National Institute of Health, USA) and Origin (Origin-Lab Corporation, MA, USA) software packages.

3 RESULTS

The spatial resolution of the system was evaluated by computing the MTF along the tube-motion direction. The MTFs for SM_{15} and SM_{40} are shown in Fig 4. The MTF associated to SM_{40} images resulted higher with respect to the MTF of SM_{15} for all spatial frequencies. Table (1) summarises the spatial frequency values corresponding to 50%, 20% and 10% of MTF curves of Fig. 4.

Table 1: Spatial frequency values corresponding to $MTF_{50\%}$, $MTF_{20\%}$ and $MTF_{10\%}$ for SM_{15} and SM_{40} images respectively. The presented values were extracted from MTF curves shown in Fig. 4.

	SM_{15}	SM_{40}
Nyquist Frequency (mm^{-1})	3.3	5.0
$MTF_{50\%}$ Frequency (mm^{-1})	1.7	2.7
$MTF_{20\%}$ Frequency (mm^{-1})	2.6	4.0
$MTF_{10\%}$ Frequency (mm^{-1})	3.1	4.8

Tables (2) and (3) show the results for CNR calculation obtained for low contrast inserts of the ACR and the TORMAM phantom respectively.

Table 2: CNR values for SM_{15} and SM_{40} images, calculated for four larger masses of the ACR phantom.

Insert size (mm)	CNR SM_{15}	CNR SM_{40}
2	4.4 ± 0.8	2.0 ± 0.1
1	3.0 ± 0.4	1.0 ± 0.2
0.75	2.5 ± 0.1	1.2 ± 0.2
0.5	1.8 ± 0.6	0.9 ± 0.2
0.25	Not visible	Not visible

A lower number of the TORMAM phantom low-contrast inserts were clearly identifiable in SM_{40} images (Table 3), hence they were excluded from our analysis. At the same time, the mass corresponding to 0.25 mm of thickness of ACR phantom was detectable neither in SM_{15} nor in SM_{40} images, while the other masses were clearly visible in both modalities (Table 2). Both for ACR and TORMAM analysis, the CNR values obtained for the SM_{15} resulted higher with respect to those obtained in SM_{40} images for all the analyzed inserts. It is possible to observe a clear trend in these values: more in detail, the CNR values related to SM_{15} images were always about twice than CNR values related to SM_{40} images, for most of the inserts of the two phantoms. These results are mainly due to a significant difference in terms of the standard deviation values of the background which resulted higher (approximately twice) for SM_{40} with respect to SM_{15} images. Conversely, the mean pixel value was roughly the same in both acquisition modes.

The radial NPS obtained from SM_{15} and SM_{40} images are shown in Fig. 5. It is possible to emphasize some similarities and some differences in the obtained NPS curves: firstly, both NPS curves show the same trend (i.e. the presence of a peak at low frequencies and a fall-off at high spatial frequencies). However, the magnitude of the two curves is significantly different: since the area under the NPS curve is proportional to the square of the image noise (standard deviation calculated in a ROI), the SM_{40} images result affected by a higher noise than SM_{15}.

Table 3: CNR values for SM_{15} and SM_{40} images, calculated for the 6 groups of low contrast inserts of the TORMAM phantom.

Insert group	Insert type	CNR SM_{15}	CNR SM_{40}
1	B	4.6 ± 0.9	2.1 ± 0.4
	A	4.3 ± 0.5	2.3 ± 0.3
	C	1.3 ± 0.3	0.8 ± 0.2
2	C	2.0 ± 0.7	1.0 ± 0.2
	B	3.8 ± 0.9	1.9 ± 0.3
	D	1.6 ± 0.4	0.6 ± 0.5
3	D	1.1 ± 0.2	0.4 ± 0.1
	C	1.5 ± 0.1	1.1 ± 0.2
	E	1.1 ± 0.1	Not visible
4	E	2.8 ± 0.6	Not visible
	D	1.6 ± 0.6	1.3 ± 0.2
	F	Not visible	Not visible
5	A	6.1 ± 0.7	3.3 ± 0.2
	F	Not visible	Not visible
	B	3.9 ± 0.4	2.4 ± 0.2
6	F	Not visible	Not visible
	E	0.8 ± 0.3	Not visible
	A	5.6 ± 0.2	2.7 ± 0.1

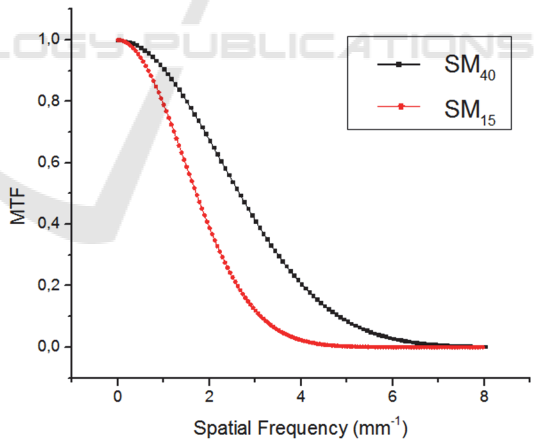

Figure 4: MTFs computed through the LSF method both for SM_{15} and SM_{40} images. LSFs were extracted from a 12.5 µm diameter tungsten wire tilted by about 3° (Fig. 1).

Fig. 6 presents normalised SNR maps related to SM_{15} and SM_{40} images. Clear differences in the non-uniformity pattern of the two SNR maps can be observed. A quantitative comparison was done by computing the NUI: values of 0.40 and 0.26 were found for SM_{15} and SM_{40} respectively (i.e. SM_{40}

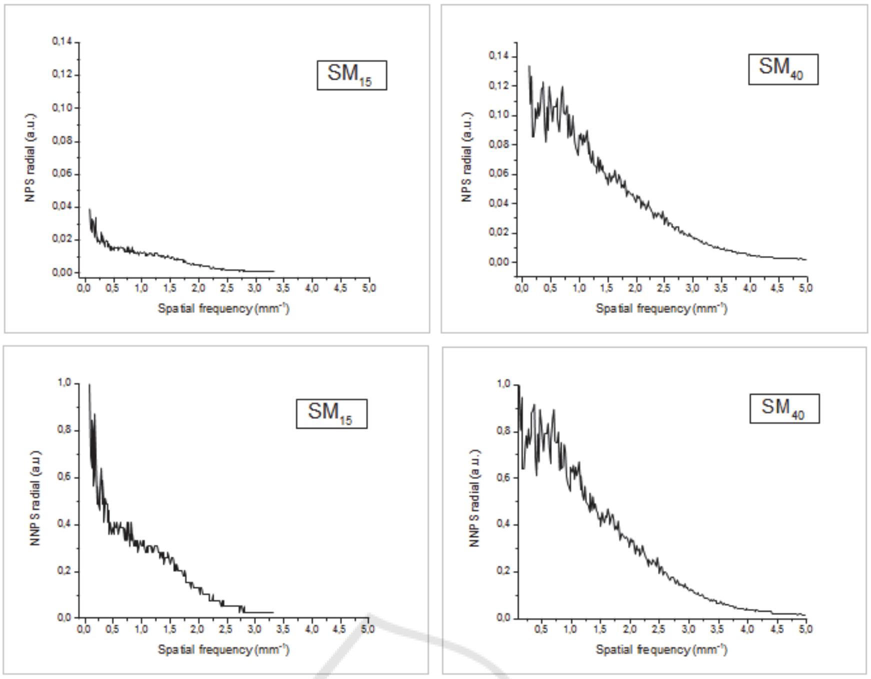

Figure 5: Examples of radial NPS and the normalized radial NPS (NNPS) for SM_{15} (on the left) and SM_{40} (on the right) images respectively. The NNPS was computed by normalizing the NPS to the maximum value.

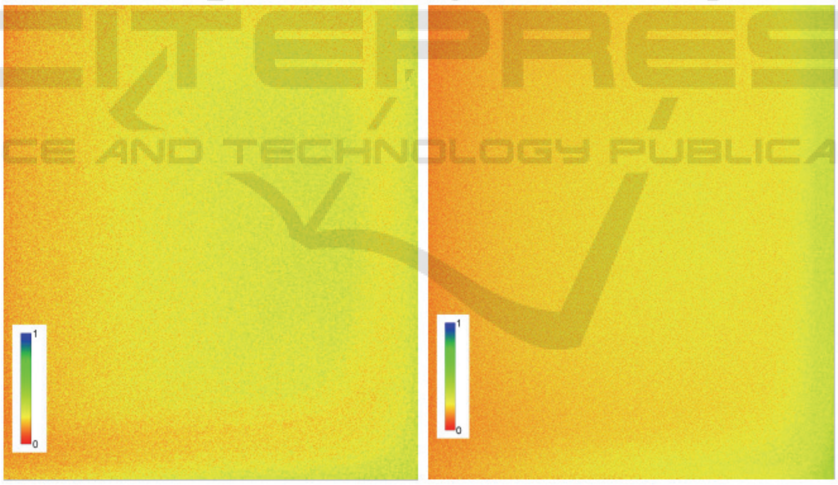

Figure 6: SNR maps obtained from 30 images of the homogeneous PMMA phantom acquired in the same conditions for SM_{15} (on the left) and SM_{40} (on the right) images. The image dimensions were 21.6 x 27.6 cm^2. The maps were normalised to the maximum value in order to obtain a better visualisation of SNR distribution across the image.

images resulted more homogeneous in terms of SNR spatial distribution).

4 DISCUSSION

The synthesized mammograms were recently introduced in the clinical practice with the goal of reducing additional breast dose due to an extra DM acquisition in DBT examinations. The possibility of replacing the DBT+DM acquisition with DBT+SM is currently being evaluated by comparing the image quality in both modalities. Although SMs exhibit different image quality properties as compared to DM images, a number of qualitative and semi-quantitative studies have highlighted similar results in clinical performance for both modalities (Alshafeiy et al., 2017; Zuley et al., 2018; Zuckerman et al., 2016; Wahab et al., 2018; Murphy et al., 2018). In addition, few studies have objectively compared some aspects of SM and DM image quality finding different and contrasting results. Therefore, to date, it is not clear if SMs could completely replace the DM images (Nelsen et al., 2016; Ikejimba et al., 2016; Baldelli et al., 2018; Barca et al., 2019).

However, the SMs represent a useful diagnostic support to DBT images, especially for wide-angle DBT which is characterized by a better spatial resolution in depth but also by worse performance in detecting microcalifications with respect to narrow-angle DBT and DM (Marshall et al., 2012; Yoshinari et al., 2014; Chan et al., 2014; Hadjipanteli et al., 2016; Rodriguez-Ruiz et al., 2016; Rose et al., 2013; Hadjipanteli et al., 2017).

For these reasons, in this phantom study we aimed to study how the image quality of the SMs was influenced by different X-ray tube angular range (15° and 40°). Spatial resolution, contrast and noise properties of phantom images were assessed.

Specifically, the spatial resolution of the system was evaluated by computing the MTF. Our results showed a better performance of SM_{40} with respect to the SM_{15}. In fact, the MTF related to SM_{40} images resulted higher with respect to the MTF of SM_{15} over all the spatial frequencies. These results are probably due to the larger pixel size in SM_{15} images than SM_{40} (0.15 mm for SM_{15} and 0.10 mm for SM_{40} images in our case). In fact, even the projection images express higher MTF in HR mode than ST mode (National Health Service UK, 2018). Notice that our mammographic device allowed to obtain SM images only with these fixed parameters (i.e. fixed values of pixel sizes and fixed number of projections for both modalities). It would be interesting to investigate how the resolution properties of the system are influenced by varying the number of projections and by using the same pixel size.

The CNR values were evaluated for the four larger masses of the ACR phantom and for the low-contrast inserts of the TORMAM phantom. Higher values were found for SM_{15} images with respect to SM_{40} for all analyzed inserts; besides, a lower number of inserts resulted visible in SM_{40} images analysis. Therefore, wide-DBT expresses worse performance in the detection of low-contrast details: this aspect could be mainly due to a greater presence of noise in SM_{40} images than in SM_{15}, as has been confirmed by evaluating the standard deviation values in both the images and by the NPS results. Notice that the number of projections acquired is the same in both modalities. It follows that in HR mode each acquisition is performed after a wider angular step; this could partially explain why SM_{40} images express higher noise with respect to SM_{15}.

Noise properties of the SM_{15} and SM_{40} images were also investigated through the calculation of the NPS. More in detail, the NPS curves obtained in the two acquisition modes exhibit the same trend, characterized by the presence of a peak at low frequencies and by a fall-off at high spatial frequencies. However, the magnitude of the two curves is significantly different: the area under the SM_{15} NPS curve results lower than that of SM_{40} one, in agreement with the standard deviation values found for CNR calculation.

SNR spatial distribution was evaluated by computing SNR maps. From a first visual inspection, a different distribution of SNR can be observed. This spatial distribution was then quantified by calculating the NUI: values of 0.40 and 0.26 were found for SM_{15} and SM_{40} respectively. In addition, SM_{40} are characterized by lower SNR values with respect to SM_{15} (Fig. 6): this is related to the previous mentioned results in terms of noise magnitude of the two modes.

5 CONCLUSIONS

In this phantom study, the image quality of SM_{15} and SM_{40} was evaluated in terms of several parameters. Better spatial resolution performance was found for SM_{40} while higher CNR values were obtained for SM_{15}, which also showed a lower noise magnitude. No differences in NPS dependence as a function of the spatial frequency were found in both modes, while different pattern of SNR distribution were observed. Even though further studies are required in terms of contrast-detail analysis and detectability assessment, this work could help to better interpret the implication of the choice between the two modalities as well as the quality of SM images obtained at different angular ranges on a specific DBT system.

ACKNOWLEDGMENTS

The presented work is part of the RADIOMA project which is partially funded by "Fondazione Pisa", Technological and Scientific Research Sector, Via Pietro Toselli 29, Pisa.

REFERENCES

Sechopoulos I. 2013. A review of breast tomosinthesis. Part I. The image acquisition process. *Med Phys; 40(1):014302*

Sechopoulos I. 2013. A review of breast tomosinthesis. Part II. Image reconstruction, processing, analysis, and advanced applications. *Med Phys; 40(1):014302*

Vedantham S, Karellas A, Vijayaraghavan GR, Kopans DB. 2015. Digital breast tomosynthesis: state of the art. *Radiology; 277(3): 663-684*

Marshall NW, Bosmans H. 2012. Measurements of system sharpness for two digital breast tomosynthesis systems. *Phys. Med. Biol. (57) 7629-7650*

Yoshinari ODA, Takaaki ITO, Keiichiro SATO, Morita J. 2014. Development od Digital Mammography System "AMULET Innovality" for examining breast cancer. *Fujifilm research & development (No.59)*

Chan HP, Helvie MA, Hadjiisky L, Jeffries DO et al. 2017. Characterization of breast masses in digital breast tomosynthesis and digital mammograms: an observer performance study. *Acad Radiol; 24(11):1372-1379*

Chan HP, Goodsitt M, Helvie MA, Zelakiewicz S et al. 2014. Digital Breast Tomosynthesis: observer performance of clustered microcalcification detection on breast phantom images acquired with an experimental system using variable scan angles, angular increments and number of projection views. *Radiology 273(3)*

Hadjipanteli A, Elangovan P, Looney P, Mackenzie A, Wells K, Dance DR, Young KC. 2016. Detection of microcalcification clusters in 2D-Mammography and Digital Breast Tomosynthesis and the relation to the standard method of measuring image quality. *XIV Mediterranean Conference on Medical and Biological Engineering and Computing 2016, IFMBE Proceedings 57, DOI: 10.1007/978-3-319-32703-7_44*

Mackenzie A, Marshall NW, Hadjipanteli A, Dance DR, Bosmans H, Young KC. 2017. Characterisation of noise and sharpness of images from four digital breast tomosynthesis systems for simulation of images for virtual clinical trials. *Phys. Med. Biol. (62):2376-2397*

Rodriguez-Ruiz A, Castillo M, Garayoa J, Chevalier M. 2016. Evaluation of the technical performance of three different commercial digital breast tomosynthesis systems in the clinical environment. *Med Phys; 32(6):767-777*

Rose SL, Tidwell AL, Bujnoch LJ, Kushwaha AC, Nordmann AS, Sexton R. 2013. Implementation of breast tomosynthesis in a routine screening practice: an observational study. *AJR Am J Roent genol.;200(6):1401–8*

Hadjipanteli A, Elangovan P, Mackenzie A, Looney PT, Wells K et al. 2017. The effect of system geometry and dose on the threshold detectable calcification diameter in 2D-mammography and digital breast tomosynthesis. *Phys. Med. Biol. 62:858-877*

Houssami N. 2018. Evidence on Synthesized Two-dimensional Mammography Versus Digital Mammography When Using Tomosynthesis (Three-dimensional Mammography) for Population Breast Cancer Screening. *Clinical Breast Cancer 18(4):, 255-260.e1*

Shin SU, Chang JM, Bae MS, Lee SH, Cho N, Seo M, Kim WH, Moon WK. 2014. Comparative evaluation of average glandular dose and breast cancer detection between single-view digital breast tomosynthesis (DBT) plus single-view digital mammography (DM) and two-view DM: correlation with breast thickness and density. *Eur Radiol;25(1): 1-8*

Svahn T, Andersson I, Chakraborty D, Svensson S, Ikeda D, Förnvik D, Mattsson S, Tingberg A, Zackrisson S. 2010. The diagnostic accuracy of dual-view digital mammography, single-view breast tomosynthesis and a dual-view combination of breast tomosynthesis and digital mammography in a free-response observer performance study. *Radiat Prot Dosim; 139(1-3):113-117*

Durand MA. 2018. Synthesized Mammography: Clinical Evidence, Appearance, and Implementation. *Diagnostics*; 8(2).pii:E22

Zuckerman SP, Maidment ADA, Weinstein SP, McDonald E.S, Conant EF. 2017. Imaging With Synthesized 2D Mammography Differences, Advantages, and Pitfalls Compared With Digital Mammography. *AJR; 209(1):222–229*

Alshafeiy TI, Wadih A, Nicholson BT , Rochman CM, Peppard HR, Patrie JT, Harvey JA. 2017. Comparison Between Digital and Synthetic 2D Mammograms in Breast Density Interpretation. *AJR Am J Roentgenol.;209(1):W36-W41*

Smith A. Synthesized 2D Mammographic Imaging - Theory and Clinical Performance. C-View White Paper. Available online: www.lowdose3d.com/images/C-View-White Paper.pdf (accessed on 1 November 2018)

EUREF. 2006. European guidelines for quality assurance in breast cancer screening and diagnosis. Fourth edition.

EUREF. 2016. Protocol for the Quality Control of the Physical and Technical Aspects of Digital Breast Tomosynthesis Systems.

EFOMP. 2015. Mammo Protocol. Quality controls in digital mammography - Protocol of the EFOMP mammo working group.

Fluke Biomedical. 2005. Mammographic Accreditation Phantom Operators Manual, Manual No. 18-220-1 Rev. 2

Goodsitt MM, Chan HP, Schmitz A, Zelakiewicz S, Telang S, Hadjiiski L et al. 2014. Digital breast tomosynthesis: studies of the effects of acquisition geometry on contrast-to-noise ratio and observer preference of low-contrast objects in breast phantom images. *Phys Med Biol 59(19):5883-902*

Siewerdsen JH, Cunningham IA and Jaffray DA. 2002. A framework for noise-power spectrum analysis of multidimensional images. *Medical Physics; 29(11):2655-71*

Zuley ML, Guo B, Catullo VJ, Chough DM, Kelly AE et al. 2014). Comparison of two-dimensional synthesized mammograms versus original digital mammograms alone and in combination with tomosynthesis images. *Radiology 271(3):664-71*

Zuckerman SP, Conant EF, Keller BM et al. 2016. Implementation of synthesized two-dimensional mammography in a population-based digital breast tomosynthesis screening program. *Radiology 281(3):730-6*

Wahab RA, Lee SJ, Zhang B, Sobel L, Mahoney MC . 2018. A Comparison of full-field digital mammograms versus 2D synthesized mammograms for the detection of microcalcifications on screening. *Eur J Radiol. 107:14-19*

Murphy MC, Coffey L, O'Neill AC, Quinn C, Prichard R McNally S. 2018. Can the synthetic C view images be used in isolation for diagnosing breast malignancy without reviewing the entire digital breast tomosynthesis data set?. *Ir J Med Sci 187(4): 1077-81*

Nelsen JS, Wells JR, Baker JA, Samei E. 2016. How does c-view image quality compare with conventional 2D FFDM?. *Med. Phys. 43(5):2538*

Ikejimba LC, Glick SJ, Samei E, Lo JY. 2016. Assessing task performance in FFDM, DBT and synthetic mammography using uniform and anthropomorphic physical phantoms. *Med. Phy. 43(10):5593*

Baldelli P, Bertolini M, Contillo A, Della Gala G, Golinelli P, Pagan L, Rivetti S, Taibi A. 2018. A comparative study of physical image quality in digital and synthetic mammography from commercially available mammography systems. *Phys Med Biol;63(16):165020*

Barca P, Lamastra R, Aringhieri G, Tucciariello RM, Traino AC, Fantacci ME. 2019. Comprehensive assessment of image quality in synthetic and digital mammography: a quantitative comparison. *Australas Phys Eng Sci Med DOI 10.1007/s13246-019-00816-8*

National Health Service UK. 2018. Technical evaluation of Fujifilm AMULET Innovality digital breast tomosynthesis system. *NHS Breast Screening Programme equipment report.*